RhoA activation promotes ordered membrane domain coalescence and suppresses neuronal excitability

Soheila Sabouri[1,#], Lucas J. Handlin[1,#], Natalie L. Macchi[1], Nicolas L.A. Dumaire[2], Aubin Moutal[2], and Gucan Dai[1*]

[1]Edward A. Doisy Department of Biochemistry & Molecular Biology, Saint Louis University School of Medicine, 1100 South Grand Blvd., St. Louis, MO, 63104

[2]Department of Pharmacology and Physiology, Saint Louis University School of Medicine

[#]Equal Contributions

[*]Corresponding Author: Gucan Dai (gucan.dai@health.slu.edu)

ABSTRACT

This study explores how the small GTPase RhoA modulates plasma membrane lipid nanodomains, particularly cholesterol-rich ordered membrane domains (OMDs). These nanodomains play a critical role in regulating ion channel activity and neuronal excitability. However, due to their nanoscale dimensions, OMDs remain challenging to visualize using conventional light microscopy. Here, we used fluorescently labeled cholera toxin B (CTxB) and the palmitoylated peptide Lck-10 (L10) as probes to visualize OMDs and quantified their size via confocal fluorescence lifetime imaging microscopy (FLIM)-based Förster resonance energy transfer (FRET). Pharmacological inhibition of RhoA significantly reduced OMD sizes in both human cell lines and dorsal root ganglion (DRG) neurons. To achieve better spatiotemporal control of specific RhoA activation, we employed an improved light-inducible dimerization (iLID) system. Optogenetic activation of RhoA rapidly increased FRET efficiency between CTxB probes, indicating OMD coalescence. Functionally, RhoA inhibition potentiated hyperpolarization-activated cyclic nucleotide-gated (HCN) channel activity in nociceptive DRG neurons, increasing spontaneous action potential firing. Conversely, in a spared nerve injury rat model, RhoA activation expanded OMDs in nociceptive DRG neurons. Constitutive RhoA activation suppressed HCN channel activity and decreased membrane excitability. These findings support a neuroprotective role for RhoA activation, where it restores OMD size and suppresses pathological hyperexcitability in neuropathic pain.

INTRODUCTION

Cell membranes are laterally heterogenous, composed of lipid domains that vary in composition and size and act as platforms for localized cell signaling (1, 2). One major type of domain, termed liquid ordered (L_o) or ordered membrane domain (OMD), is characterized by its high levels of cholesterol and sphingolipids. OMDs vary in size and tend to be thicker than liquid disordered (L_d) or disordered membrane domains (3-5). They have the dynamic ability to coalesce into larger or separate into smaller domains (4). Given the nanoscale size of OMDs, conventional optical microscopy cannot be used due to its resolution limit of 250 nm (1). Techniques such as Förster resonance electron transfer (FRET), stimulated emission depletion (STED) nanoscopy, and cryo-electron tomography have been used to study the structure and function of OMDs, but the dynamic behavior of OMDs in living cells remains poorly understood (3, 6-8). Importantly, lipid domains have been associated with many biological processes, including Alzheimer's disease (9-11), viral infections (12, 13), immune signaling (1, 14), and neuropathic pain (7, 15). We recently discovered that there are cell type-dependent variations in the size of OMDs, where electrically active cell types such as small DRG neurons and cardiac pacemakers may contain larger OMDs (7). These findings suggest that a high abundance of OMDs within the membrane supports and protects repetitive action potential firing. Given their critical role in normal cellular function, it is essential to identify key regulators that govern OMD dynamics.

RhoA, a small monomeric GTPase belonging to the Ras superfamily, has numerous well-known cellular functions, including regulation of actin cytoskeleton (actin stress fibers and assembly of focal adhesions), cell migration, cell shape, and endocytosis (16-19). It acts as a molecular switch in that it is inactive when bound to GDP and active when bound to GTP (16, 17). There are three types of regulatory proteins that act on RhoA: guanine nucleotide exchange factor (GEF), guanine nucleotide dissociation inhibitor (GDI), and GTPase-activating protein (GAP) (17, 20). GEFs are responsible for the exchange of GDP for GTP and therefore activate RhoA, while GAPs stimulate GTP hydrolysis and convert RhoA to its inactive form. Inactive, GDP-bound RhoA is predominantly cytosolic, often stabilized by GDI, whereas active, GTP-bound RhoA associates with the plasma membrane to engage downstream effectors. In contrast, RhoB mostly associates with endosome membranes whereas RhoC, structurally more similar to RhoA, localizes to the plasma membrane and tends to be dysregulated during various types of cancer (21). Importantly, RhoA activity is elevated markedly following peripheral nerve injury, important for nerve regeneration (22). Cytokines, particularly those involved in neuroinflammation after nerve damage (e.g., TNF-α and IL-1β), stimulate GEFs to promote RhoA signaling in neurons (23-25). In addition, following nerve injury, myelin-derived proteins such as myelin-associated glycoprotein (MAG) and Nogo-A, as well

as signaling lipid sphingosine-1-phosphate (S1P), also activate RhoA in periphery neurons (24, 26, 27). In summary, RhoA is a membrane-associated small GTPase best known for its roles in cytoskeletal regulation and intracellular signaling. However, its potential influence on the biophysical properties or organization of the lipid bilayer itself remains poorly understood.

This study is motivated by emerging evidence implicating small G protein activation in an OMD-dependent, clathrin/dynamin-independent type of endocytosis known as OMD endocytosis (OMDE) or massive endocytosis (MEND) (28-32). Upon stimulation by various types of cell stress, the plasma membrane reorganizes to coalesce OMDs which subsequently serve as sites for initiating endocytosis (29, 31, 33). OMDE is capable of rapidly recycling more than 50% of the plasma membrane (31). Overall, OMDE is enhanced by supplementation with pyruvate, moderate concentration of palmitate/albumin complexes, and calcium transients, and is inhibited by fatty acid deprivation, treatment with 2-bromopalmitate/albumin complexes, mitochondrial permeability transition pore (PTP) blockade, and inhibition of palmitoyl acyltransferases (e.g., DHHC enzymes) (28-31, 33). How actin cytoskeleton regulates OMDE remains less understood (29, 31-33). Furthermore, low concentrations of nonionic detergents (e.g. Triton X-100) have been shown to induce OMDE/MEND (29, 33), and we showed that they promote the coalescence of OMDs (7), strengthening the relationship between OMD expansion and initiation of OMDE. Given the involvement in cytoskeleton remodeling, RhoA activation and OMDE (31), we aimed to define the effects of RhoA activation on OMD properties.

We used fluorescence lifetime imaging microscopy (FLIM) combined with Förster resonance energy transfer (FRET) to investigate how RhoA activity influences OMD size. Optogenetic activation of RhoA was achieved using an improved light-inducible dimerization (iLID) system. We provide evidence supporting that RhoA activation promoted the coalescence and expansion of OMDs, whereas pharmacological inhibition of RhoA reduced OMD size in both human cell lines and primary cultured rat dorsal root ganglion (DRG) neurons. Notably, RhoA inhibition also altered ion channel activity and action potential firing in DRG neurons, likely via its effects on OMDs. Inhibition of the HCN activity by RhoA activation and the resulting dampening of membrane hyperexcitability may have evolved as an adaptation to chronic pain. These findings reveal a potential mechanistic link between small GTPases, cytoskeleton, lipid domains, and membrane excitability.

RESULTS

Effects of Rho activation and inhibition on OMD sizes, probed using FLIM-FRET

Cholera toxin subunit B (CTxB) conjugated FRET pairs were used as probes to determine relative changes in OMD size (7). These probes are pentamers derived from *Vibrio cholerae* and have a high affinity for GM1 gangliosides, a type of sphingolipid found at high levels in OMDs (34, 35). Whereas conventional fluorescence microscopy has limitations due to the diffraction limit of light (~250 nm), FRET-based fluorescence overcomes this limitation and can visualize lipid domains with nanometer-level sensitivity (7). Specifically, we used Alexa Fluor 488 (AF488) CTxB conjugates as the FRET donor and Alexa Fluor 647 (AF647) CTxB conjugates as the FRET acceptor. This pair has been previously established and validated, with a Förster critical distance (R_0) value around 52 Å (36). The radius of the lipid domain determines how many CTxB probes can be accommodated within the same lipid domain. OMDs with a radius exceeding 10 nm have a high probability of accommodating multiple CTxB probes, whereas those with a smaller radius than 10 nm can only accommodate a single probe (7, 35). A higher FRET efficiency value is therefore indicative of a larger OMD size, allowing the CTxB FRET pair to detect relative changes in OMD size (7).

Live-cell time-resolved FLIM imaging was used to quantify FRET efficiency that reported OMD sizes in tsA-201 (a variant of HEK293T) cells (7). The frequency-domain lifetime information corresponding to each image pixel in the confocal image was transformed into a pixel on a complex plane coordinate, or a phasor plot (Fig.1 A, B) (37). As we demonstrated previously, this phasor plot displays a semicircular shape, which serves as a reference for pure single-exponential lifetimes (7, 38). Multiexponential lifetimes are found within the boundaries of this semicircle. Shorter lifetimes exhibit clockwise movements along the semicircle, indicating increased FRET. This phasor approach has several advantages, such as unbiased measurement of fluorescence lifetimes without need for exponential fitting, and the ability to map multiple cursors to identify distinct lifetime species in confocal images (37, 39-41). We supplemented the CTxB conjugates at a concentration of 10 nM into the cell culture medium of tsA cells. With the addition of both FRET donor (CTxB-AF488) and acceptor (CTxB-AF647), there was a clockwise shift towards a shorter lifetime compared to the donor-only lifetime, indicating the occurrence of FRET (Fig. 1A). To calculate FRET efficiency, we used the FRET trajectory method on the phasor plot. The FRET trajectory started at the zero FRET efficiency position, aligned with the donor-only cursor, and moved through the measured phasor species. As previously demonstrated and reproduced here (7), this CTxB-based FRET efficiency was 8.8 ± 1.1% for tsA-201 cells (Fig. 1 C, D).

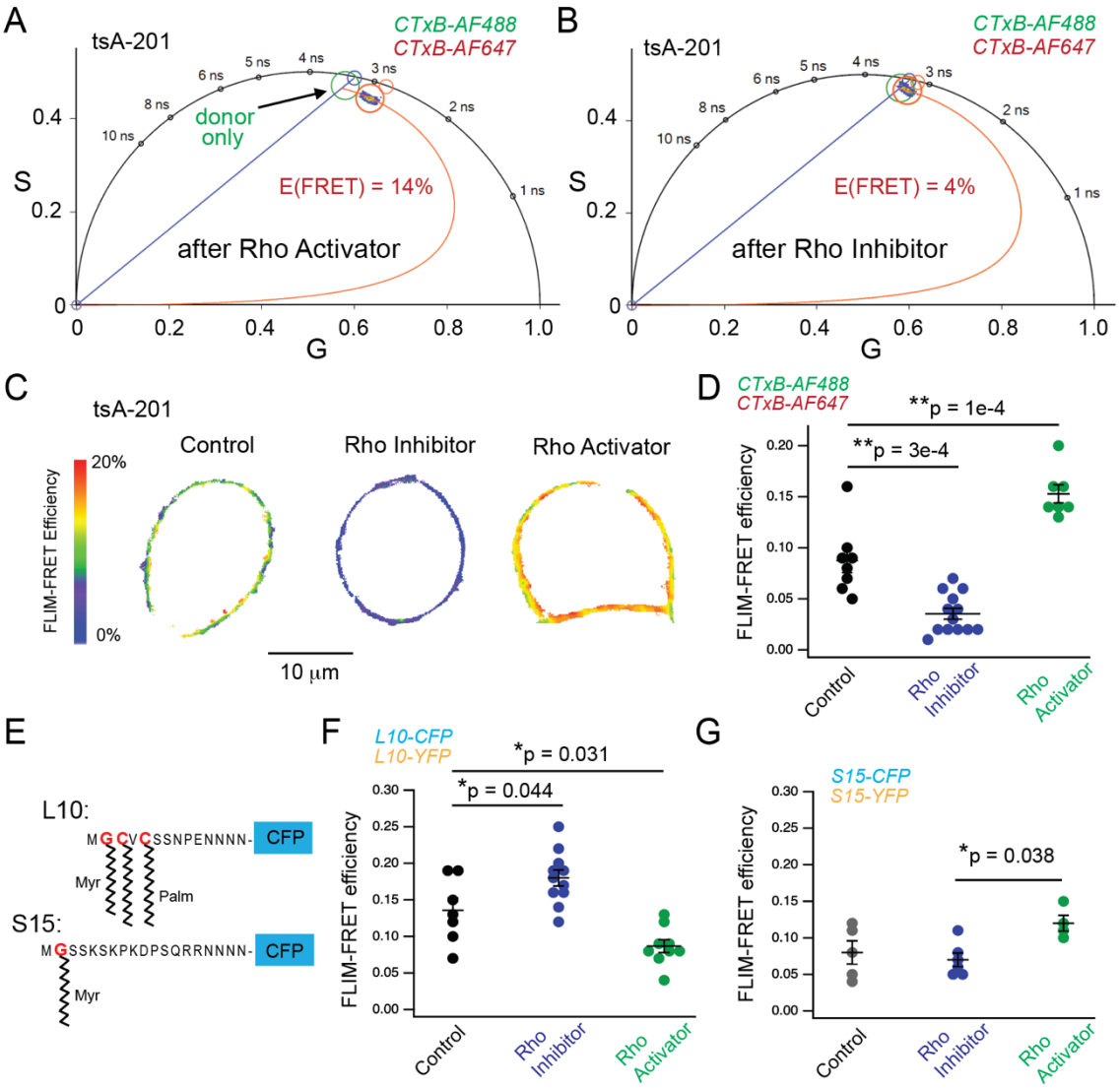

Figure 1. Rho activation increases the OMD size quantified using FLIM-FRET.
(**A-B**) Representative phasor plot of tsA-201 cells labeled by CTxB-AF488 and CTxB-AF647, without (A) and with (B) treatment of Rho inhibitor. The donor alone phasor is indicated as the green cursor, obtained from cells only labeled with CTxB-AF488. The trajectory curve in red begins at 0% FRET efficiency (donor only), progresses through the measured phasor, and ends at 100% efficiency, which overlaps with the background (0,0) coordinate. (**C**) Representative FLIM-FRET based heatmap images of tsA cells illustrate the effects of Rho inhibitor and activator on the CTxB-based FLIM-FRET efficiency. (**D**) Summary of effects of Rho inhibitor and activator on the CTxB-based FLIM-FRET efficiency in tsA cells as shown in panel C, n = 8 for the untreated control, n = 13 for the Rho inhibitor, and n = 7 for the Rho activator. Data are mean ± s.e.m., **P < 0.01, one-way ANOVA (no adjustment). (**E**) Schematic illustration of L10- and S15-CFP probes. (**F-G**) Summary of analogous experiments testing the Rho inhibitor and activator on the L10-based (n = 7 – 11 cells, panel F) or S15-based (n = 4 – 6 cells, panel G) FLIM-FRET efficiency in tsA cells. Data are mean ± s.e.m., *P < 0.05, one-way ANOVA (no adjustment).

We found that treatment with purified exoenzyme C3 transferase (1 μg/mL, > 4 hrs), a specific Rho inhibitor, significantly reduced CTxB-based FRET efficiency in tsA cells. C3 transferase, derived from *C. botulinum*, inhibits Rho GTPases through ADP-ribosylation of the effector-binding domain (42, 43).

Following treatment, the FRET efficiency decreased to 3.5 ± 0.5% (Fig. 1 B-D), indicating a disruption or dispersion of OMDs. To examine the effect of Rho activation, we applied CN03 (1 μg/mL, > 4 hrs), a Rho activator derived from bacterial cytotoxic necrotizing factor (CNF) toxins that deamidates residue Q63 in the switch II region of Rho GTPases (44, 45). This modification converts glutamine to glutamate, preventing intrinsic and GAP-stimulated GTP hydrolysis and thus maintaining Rho in a constitutively active state (44, 45). CN03 is specific to RhoA and does not modify other Ras family GTPases like Rac and Cdc42 (44, 45). CN03 treatment markedly increased FRET efficiency to 15.3 ± 0.9% (Fig. 1 C, D), suggesting expansion of OMDs. These effects probably depended on endogenous, plasma membrane–localized RhoA (P61586; intensity: 6.43), which is expressed at a higher level than endosome-localized RhoB (P62745; intensity: 4.89), and RhoC (P08134; intensity: 5.88) in HEK293 cells, according to data from ProteomicsDB (46). Together, these results suggest that RhoA activity modulates OMD organization in tsA cells—activation promotes domain coalescence, while inhibition leads to domain disruption.

To further assess changes in OMD organization during Rho activation, we performed FLIM-FRET using L10-CFP and L10-YFP, a FRET pair that preferentially partitions into OMDs (7, 47, 48). L10 refers to a probe derived from the first 10 amino acids of the Lck kinase, which contains two palmitoylation sites and targets to OMDs (Fig. 1E). Unlike the CTxB-based probes—where increased FRET reflected domain coalescence and higher chance for CTxB to bind to the membrane—the L10-based system reports decreased FRET as an indicator of OMD expansion, due to increased spacing between OMD-anchored L10 probes as OMDs grow (7, 47). We observed that the L10-based FRET increased following Rho inhibitor treatment and decreased with Rho activator treatment (Fig. 1F), further supporting the role of RhoA activation in OMD expansion. As an additional test, we used the FRET pair S15-CFP and S15-YFP, which localize to disordered membrane regions outside of OMDs (7, 47, 48). This is because the S15 probe, derived from the first 15 amino acids of the Src kinase, contains only a single myristoylation site (Fig. 1E). FLIM-FRET changes in the S15-based CFP/YFP pair were less pronounced following treatment with Rho activators or inhibitors, compared to the L10-based FRET changes, suggesting that Rho activity has a more indirect impact on disordered membrane regions (Fig. 1G).

Optogenetic activation of RhoA reveals its effect on OMDs

Pharmacological agents, which often have off-target effects on related GTPases such as RhoB and RhoC. We further used an improved Light-inducible Dimerization (iLID) system that activates RhoA specifically in a reversible manner (Fig. 2) (49-51). This improved optogenetic system has several advantages over chemical dimerization systems and previous versions of light-induced systems,

including shorter onset kinetics, smaller size, and the ability to be turned on and off (50, 52, 53). The iLID system is fast inducible, with a high recruitment efficiency and a high sensor localization to the plasma membrane (51, 52, 54). The system colocalizes within seconds following blue light excitation and reverts to the dark state within minutes (49). This optogenetic approach has previously been used to study other monomeric G proteins (49, 55), and has specifically been used to investigate the role of RhoA signaling in cell migration (51) and endothelial barrier strength (52).

The iLID optogenetic system involves the optical stimulation of a RhoA-selective GEF (Fig. 2 A, B). Specifically, there is a blue light-dependent interaction between a protein SspB and its peptide binding target SsrA. The mCherry-tagged SspB is fused to a RhoA-selective GEF, in this case the DHPH domain of LARG (56), and SsrA is fused to the blue light sensitive LOV2 domain (iLID-Caax), which is targeted to the membrane via the Caax anchor motif (49). Upon 488 nm light excitation, the LOV2 domain, specifically the J_α helix, changes conformation so that SsrA becomes available for binding by SspB (57). This allows for LARG to translocate to the membrane and activate RhoA. LARG preferentially activates RhoA over RhoB and RhoC and does not activate other Rho family proteins (58). We confirmed blue-light induced LARG translocation through visualization of increased membrane-localized mCherry fluorescence following photoactivation (Fig. 2B). The mCherry translocation from the cytosol to the membrane quickly, with a time constant of ~10 seconds (Fig. 2C). FLIM-FRET between CTxB-AF488 and CTxB-AF647 was measured during photoactivation of the cell, which was carried out over 30-time frames, each lasting approximately 7 seconds. In this protocol, the 488 nm laser served a dual purpose: activating the optogenetic system and exciting the FRET donor CTxB-AF488. We found the FRET efficiency significantly increased following endogenous RhoA activation, on average around 8% (Fig. 2 D-F). There was an exponential increase that has a time constant of ~70 seconds (Fig. 2E). Control cells lacking LARG-mCherry-SspB (untransfected) or iLID-CaaX (no mCherry translocation upon photoactivation) exhibited only a modest average increase of 1.8% in FRET efficiency (Fig. 2F). These results indicate that activation of endogenous RhoA in tsA201 cells promotes the expansion of OMDs.

We also tested the iLID system and effects on OMDs using the L10-based FRET pairs in tsA cells. As in the CTxB experiments, photoactivation was applied over 30-time frames using 445 nm light, which simultaneously activated the optogenetic system and excited the FRET donor L10-CFP. Upon RhoA activation, we observed a considerable ~4% decrease in FRET efficiency between coexpressed L10-CFP and L10-YFP, with a time constant of ~70 seconds—comparable to the kinetics of the FRET increase observed for CTxB-based FRET pairs (Fig. 2 G and H). Control cells lacking LARG-mCherry-SspB translocation showed no changes in FRET (Fig. 2I). In tsA cells expressing the optogenetic system and

S15-CFP and S15-YFP FRET pairs, photoactivation induced no measurable change in S15-based FRET efficiency, indicating that the effects observed with the L10 pair are specific to changes in lipid-ordered domains. In summary, these complementary results support the conclusion that RhoA activation drives the rapid expansion of OMDs.

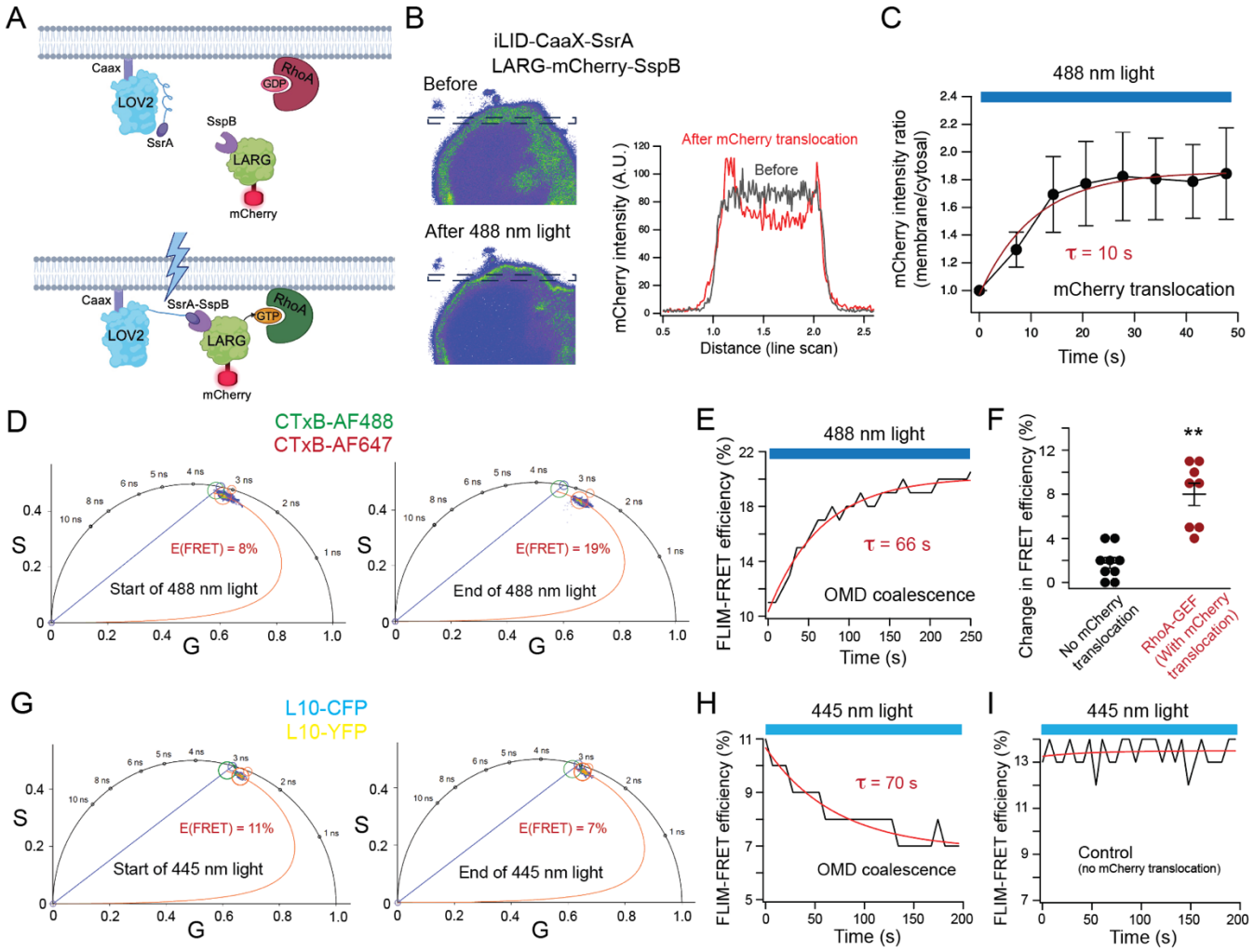

Figure 2. Activation of RhoA using an improved light-inducible dimerization (iLID) system.
(**A**) Cartoons depicting the iLID optogenetic system before and after 488 nm excitation. Upon excitation, LOV2-Caax-SsrA (blue) changes conformation to allow SspB to bind to SsrA. This prompts the RhoA-GEF LARG-mCherry-SspB (light green) to translocate to the membrane. After translocation, LARG activates RhoA (red/inactive and green/active) by exchanging GDP (red) for GTP (orange). (**B**) Representative intensity-based heatmap images of tsA-201 cells before and after 488 nm excitation. Following light excitation, mCherry fluorescence intensity increases at the membrane and decreases in the cytosol, as demonstrated by the line-scan profiles. (**C**) Time course of LARG-mCherry translocation, quantified as the fluorescence intensity ratio between membrane-localized and cytosolic signals (n = 4 cells). The data were fit with a single-exponential function, highlighted in red. (**D**) Representative phasor plots of tsA-201 cells labeled with CTxB-AF488 and CTxB-AF647 and transfected with the iLID system. Comparison of the first and 30th frames during 488 nm light excitation reveals an increase in FRET efficiency. (**E**) Representative time course of the FLIM-FRET efficiency between CTxB-AF 488 and CTxB-AF 647

during 488 nm light-induced activation of iLID system as in panel D. (**F**) Summary of FRET efficiency changes following iLID activation in cells with or without LARG-mCherry translocation. Data are presented as mean ± s.e.m.; n = 8 for cells exhibiting mCherry translocation to the plasma membrane, and n = 9 for cells without translocation, **p < 0.01, two-sided t-test. (**G**) Representative phasor plots of tsA-201 cells labeled with L10-CFP and L10-YFP and transfected with the iLID system. During the 445 nm light, FRET efficiency decreases. (**H-I**) Representative time course of the L10-based FRET efficiency between L10-CFP and L10-YFP during 445 nm light-induced activation of iLID system for tsA cells showing mCherry membrane translocation (H) versus the no-translocation control (I).

RhoA activation modulates OMD sizes in nociceptor DRG neurons and dampens membrane hyperexcitability

We extended these findings to rat primary small-diameter dorsal root ganglion (DRG) neurons, which are nociceptors responsible for detecting noxious stimuli and are highly sensitive to changes in membrane composition. These small DRG neurons are important for processing pain signals and possess larger OMDs than large-diameter DRG neurons and tsA cells (7). The FRET efficiency in naïve small DRG neurons (control) was measured at 19.5 ± 2.0% (Fig. 3 A and B). For these neurons, prolonged exposure to C3 transferase (1 μg/mL, >4 hrs) led to a significant decrease in CTxB-based FRET efficiency 10.7 ± 0.6%, consistent with a reduction in OMD sizes (Fig. 3 A and B). C3-mediated ADP-ribosylation of Rho GTPases likely disrupts cytoskeletal interactions that stabilize OMDs in the neuronal membrane. Conversely, activating Rho signaling using CN03 failed to elevate FRET efficiency significantly (measured as 20.6 ± 1.6%). This suggests that OMDs in nociceptors are large already and RhoA activation cannot further increase their sizes. Then we measured the spontaneous action potential firing of naïve nociceptor DRG neurons (Fig. 3C). In control neurons, 38% exhibited spontaneous firing (n = 13), consistent with our previously reported value of 40% (7). Spontaneous firing increased to 92% in Rho inhibitor-treated neurons (n = 13), whereas only 50% of RhoA activator-treated neurons exhibited firing (n = 10). These results suggest that, as in tsA cells, decreased RhoA activity reduces OMDs in native sensory neurons, likely modulating their excitability and signaling properties.

We next tested whether activating RhoA could restore OMD integrity in nociceptor DRG neurons isolated from rats subjected to spared nerve injury (SNI), a well-established model of neuropathic pain (59). Small-diameter neurons from SNI animals exhibited significantly reduced CTxB-based FRET efficiency (5.9 ± 1.1%) (Fig. 3D), reflecting a disruption of OMDs typically associated with chronic injury and membrane hyperexcitability (7). Treatment with Rho activator CN03 reversed this reduction, restoring FRET efficiency (16.6 ± 1.6%) toward levels observed in naïve controls (Fig. 3D). These findings suggest that RhoA signaling plays a critical role in preserving OMD architecture under pathological conditions and may offer a mechanism to stabilize membrane nanodomain organization in sensory neurons affected by

nerve injury. Notably, this normalization of OMD sizes coincided with reduced spontaneous firing: only 57% of RhoA-activated SNI neurons exhibited spontaneous activity (n = 7), compared to 100% in hyperexcitable SNI controls (n = 4), consistent with our previous findings (7) (Fig. 3E).

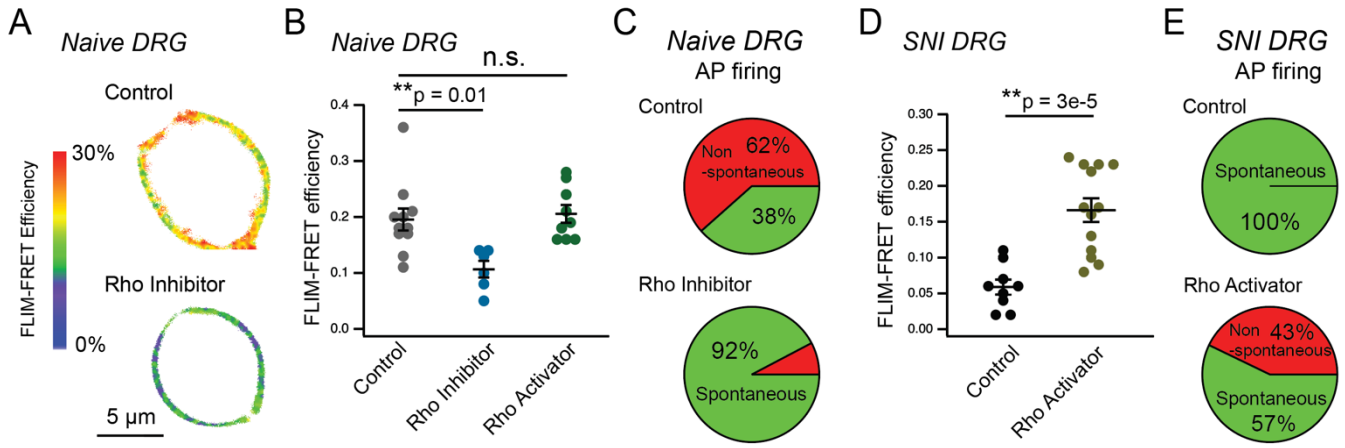

Figure 3. Rho inhibition and activation alters OMD size and membrane excitability of primary nociceptor DRG neurons.
(**A**) Representative FLIM-FRET based heatmap images of naïve small DRG cells illustrate the effect of Rho inhibitor on the CTxB-based FLIM-FRET efficiency. (**B**) Summary of the effects of Rho inhibitor and activator on the CTxB-based FLIM-FRET efficiency for naïve small DRG neurons, n = 11 for the untreated control, n = 6 for Rho inhibitor-treated neurons, and n = 9 for Rho activator-treated neurons. Data are mean ± s.e.m., one-way ANOVA (no adjustment). (**C**) Pie charts illustrating the percentage of spontaneous action potential (AP) firing of naïve DRG neurons comparing untreated control and Rho inhibitor-treated neurons; green color: spontaneous firing; red color: nonspontaneous firing. (**D**) Summary of effects of Rho inhibitor and activator on the CTxB-based FLIM-FRET efficiency for small DRG neurons from spared nerve injury (SNI) model rats, n = 9 for the untreated control, n = 13 for the Rho-activator treated. Data are mean ± s.e.m., two-sided t-test. (**E**) Pie charts illustrating the percentage of spontaneous AP firing of SNI small DRG neurons comparing untreated control and Rho activator.

Rho activation alters HCN channel function in DRG neurons via OMD-dependent mechanisms

Neuronal HCN channels are essential for supporting autonomous neuronal firing and are regulated by biophysical properties of the surrounding lipid membrane, particularly through their association with OMDs (7, 60). Disruption of OMDs—such as by cholesterol depletion using β-cyclodextrin (β-CD)—has been shown to markedly facilitate HCN channel gating, leading to faster activation and increased channel opening (7). These changes in HCN gating contribute to enhanced neuronal excitability and are characteristic of sensory neurons under chronic neuropathic pain conditions (7). In this context, we tested the role of RhoA signaling in modulating HCN channel function via OMDs. Using whole-cell patch clamp recordings, we measured native HCN currents in small-diameter DRG neurons from SNI rats by applying a series of hyperpolarizing voltage steps. To evaluate the role of RhoA

signaling, we pharmacologically activated RhoA using CN03 and compared HCN current properties with untreated controls (Fig. 4 A, B). Small SNI neurons are known to exhibit disrupted OMDs and facilitated HCN channel opening, which contribute to their increased spontaneous excitability (7). We found treatment with the Rho activator (1 μg/mL, >4 hours) partially reversed this pathological phenotype. HCN channel activation kinetics were markedly slowed, with the primary activation time constant (τ_1) increasing from 74 ± 4 ms to 103 ± 9 ms (Fig. C). In addition, the slope factor of the conductance-voltage (G-V) activation curve was reduced, consistent with the restoration of OMDs in nociceptor DRG neurons (Fig. 4 D-E). The reduced slope factor suggests increased total gating charge movement per channel during activation, consistent with membrane thickening caused by OMD coalescence (7). The half-maximal voltage ($V_{1/2}$) derived from the G-V curve for channel activation only showed an insignificant change (Fig. 4D). These findings demonstrate that RhoA activation supports OMD integrity, inhibits HCN channel function, and attenuates neuropathic hyperexcitability.

To support the OMD-mediated effect on HCN channels by RhoA, we investigated whether inhibition of RhoA might alter the channel gating in the opposite direction for naïve small DRG neurons. Naïve small DRG neurons exhibit large OMDs, and RhoA inhibition reduces their size, whereas RhoA activation does not further enlarge them (Fig. 3). As expected, we found that inhibiting RhoA with C3 transferase (1 μg/mL for ~4 hours) significantly accelerated HCN channel activation and increased the slope factor of the G-V activation curve (Fig. 4F, H), recapitulating the β-CD-induced phenomenon of OMD disruption. Similar to the effect by the RhoA activator to SNI neurons, $V_{1/2}$ of HCN activation did not change significantly after the RhoA inhibition (Fig. 4G). Together, these results demonstrate that RhoA signaling critically stabilizes OMDs to regulate HCN gating and modulate action potential firing patterns.

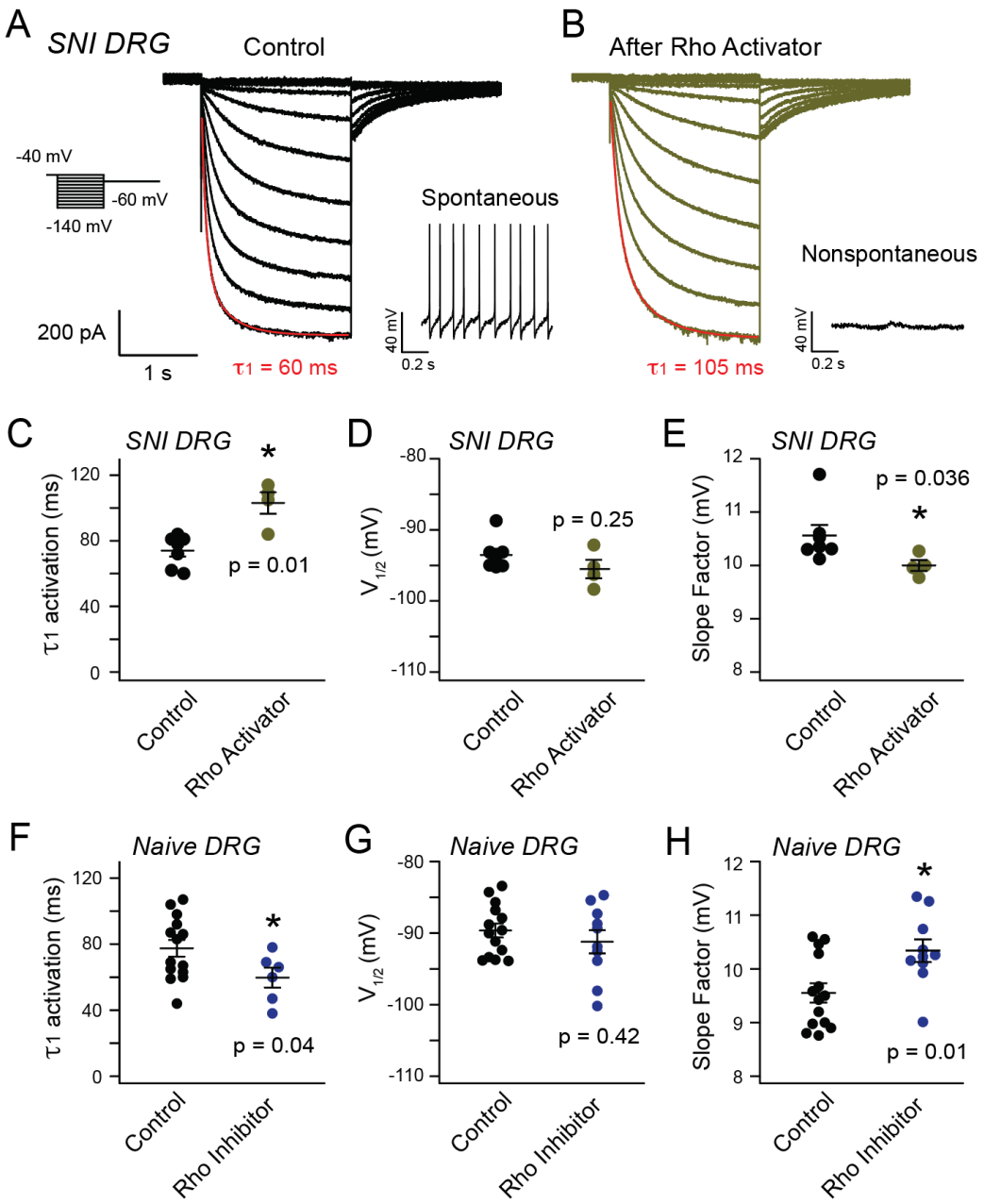

Figure 4. Rho inhibition and activation impacts HCN channel gating in nociceptor DRG neurons. (**A-B**) Representative HCN current traces illustrating that RhoA activation accelerates channel activation. Red traces indicate double-exponential fits of the current at -140 mV. Spontaneous action potentials recorded from the same SNI neuron are shown for comparison: untreated neurons (control, panel A) exhibited spontaneous firing, whereas neurons treated with the Rho activator did not (panel B). (**C-E**) Summary of the parameters from Boltzmann fit of the G-V relationship for HCN channel activation before and after the RhoA activator treatment of SNI small DRG neurons: activation time constant (τ_1) in panel C, $V_{1/2}$ in panel D and slope factor (V_s) in panel E, n = 7 patches for the control and n = 4 patches for the Rho activator condition, *p < 0.05, **p < 0.01, two-sided t-test. (**F-H**) Summary of the parameters from Boltzmann fit of the G-V relationship of HCN channel activation before and after the RhoA inhibitor treatment of naïve small DRG neurons: activation time constant (τ_1) in panel F, $V_{1/2}$ in panel G and slope factor (V_s) in panel H, n = 14 patches for the control, n = 6 for τ_1 of HCN activation under the RhoA activator condition, and n = 10 for $V_{1/2}$ and V_s of the G-V curve fits for HCN activation under the RhoA activator condition *p < 0.05, **p < 0.01, two-sided t-test.

DISCUSSION

OMDs are gaining increasing recognition for their involvement in a variety of essential cellular processes. Broadly, they function to spatially compartmentalizing membrane proteins, thereby regulating their interactions and activity (1). It has been found that many receptors involved in innate and adaptive immune responses are associated with OMDs during their active signaling (1, 14). Similarly, a multitude of proteins associated with cancer (1, 61, 62) and cardiovascular disease (1, 63) have been shown to preferentially localize to OMDs. Disturbances in OMD size, whether that be shrinking or expansion, have been linked to Alzheimer's disease (9, 10), autoimmune disorders (1, 14), and neuropathic pain (15). We previously demonstrated that the size of OMDs influences the excitability and activity of nociceptive DRG neurons, with smaller OMDs leading to increased membrane excitability and higher action potential firing frequency. This study uncovers a novel link between the GTPase RhoA and neuropathic pain by investigating how RhoA modulates OMDs. Using FLIM-FRET, we achieved nanoscale resolution to monitor relative changes in OMD size with domain-specific probes. RhoA activation significantly expanded OMDs, establishing its direct regulatory role in OMD architecture.

Considering the established roles of OMDs and RhoA, we propose that RhoA activation serves as an evolutionary protective mechanism against neuronal hyperexcitability through OMD modulation. Previously, RhoA activation was reported to influence membrane excitability by regulating the trafficking of voltage-gated ion channels (64-66). RhoA activation was also suggested to interact with IP_3 receptors to modulate calcium signaling and function of endothelial cells (67). Nevertheless, the impact of RhoA activation specifically on nociceptor DRG neurons via ion channels has not been well studied. Our findings suggest that, beyond RhoA's established role in ion channel trafficking, direct RhoA/OMD-mediated suppression of HCN channel gating may further contribute to decreased excitability in DRG neurons upon RhoA activation.

How RhoA activation promotes OMD coalescence remains less understood, but multiple lines of evidence point to both cytoskeletal remodeling and lipid-protein interactions as key mechanisms (28, 68, 69). RhoA is known for its role in actin cytoskeleton dynamics, and its activation leads to increased actomyosin contractility and cortical tension, largely through its downstream effector Rho-associated protein kinase (ROCK). Increased cortical tension can directly influence membrane mechanics and promote lateral compression of membrane domains, favoring the clustering of cholesterol- and sphingolipid-rich regions into larger, more stable OMDs (70, 71). In parallel, RhoA may promote OMD coalescence by enhancing the palmitoylation of proteins that preferentially localize to OMDs, such as

GPI-anchored proteins, caveolins, and ion channels. Palmitoylation increases the localization of membrane proteins for OMDs (11, 72, 73), and RhoA may be implicated in facilitating protein palmitoylation either directly or through downstream signaling pathways (69, 74, 75). Specifically, RhoA activity likely regulates the subcellular localization or activity of palmitoyl acyltransferases that contain DHHC domains, thereby influencing the lipidation status of OMD-resident proteins (69, 76).

Our findings support the hypothesis that RhoA plays a critical role in the noncanonical clathrin/dynamin-independent, but OMD-dependent form of endocytosis first described by Hilgemann and colleagues (28-30). In OMDE (or MEND), coalescence of OMDs precedes the formation and budding of large endocytic vesicles, often in response to metabolic or calcium stress. The proposed model posits that lipid phase separation and protein crowding within OMDs serve as initiation site for membrane invagination. Notably, the actin cytoskeleton appears dispensable in the late stages of OMDE, suggesting that lipid phase behavior and membrane tension dominate vesicle formation (30). Our observation that RhoA activation increases OMD coalescence suggests that RhoA may facilitate the initiation phase of OMDE, possibly by organizing the lipid environment and palmitoylated membrane proteins into coalesced OMDs that are competent for internalization. Altogether, these findings imply that RhoA acts as a molecular bridge between cytoskeletal forces and lipid domain dynamics, coordinating mechanical and biochemical cues that promote condensation and endocytosis events like OMDE. Future work could dissect the specific lipid and protein effectors downstream of RhoA involved in this process, potentially identifying new therapeutic targets in treating neuropathic pain where OMD dynamics are dysregulated.

MATERIALS AND METHODS

Molecular Reagents, Cell Culture, and Transfection

Frozen aliquots of tsA-201 cells, a type of human embryonic kidney HEK cell, were acquired from Sigma-Aldrich (St. Louis, MO) and stored in liquid nitrogen. Cells were cultured in Dulbecco's modified Eagle's medium (DMEM; Gibco), supplemented with 10% fetal bovine serum (FBS; Gibco) and 1% penicillin/streptomycin (Gibco), then stored in a humidified incubator at 37 degrees Celsius with 5% CO_2. Following previously established protocols (11, 77), transfection was performed on 50-90% confluent tsA-201 cells with the lipofectamine 3000 kit (Invitrogen, Carlsbad, CA, #L30000080). iLID system transfection constructs included LARG-mCherry-sspB (Addgene: #90459) and iLID-CaaX-ssrA (Addgene: #85680). DNA concentration was measured using a Nanodrop OneC spectrophotometer (Life Technologies, Grand Island, NY). The Cholera Toxin Subunit B-Alexa Fluor™ 488 and 647 conjugates were purchased from ThermoFisher Scientific and administered to cultured cells at a concentration of 10 nM for 5-10 minutes (7). L10-CFP, L10-YFP, S15-CFP and S15-YFP are gifts from Prof. Bertil Hille, University of Washington, Seattle. The membrane-permeable Rho activator II and inhibitor I were all purchased from Cytoskeleton, Inc (Denver, CO).

Fluorescence Lifetime Measurement and confocal FLIM-FRET

Digital frequency-domain fluorescence lifetime imaging (38, 78) was performed with a Q2 laser scanning confocal system equipped with a FastFLIM data acquisition module (ISS, Inc, Champaign, IL), and two hybrid PMT detectors (Model R10467-40, Hamamatsu USA, Bridgewater, NJ). An Olympus IX73 inverted microscope (Olympus America, Waltham, MA) is coupled to the confocal system. Both the frequency domain (instantaneous distortion-free phasor plotting) and time-domain decay information are included in the fluorescence lifetime measurements. Simultaneous two-color imaging was performed with dichroic cubes, one equipped with a 50/50 beam splitter and the other with various long-pass filters. A supercontinuum laser with a wavelength range of 410 to 900 nm, a repetition rate of 20 MHz, and a pulse duration of 6 ps was used for fluorescence excitation. Specifically, AF-488 was excited at 488 nm and mCherry was excited at 561 nm. To detect the emission for AF-488 and mCherry, an emission cube filter consisting of a 525/40 nm filter for AF-488, a 552 nm long-pass dichroic mirror, and a 593/40 nm filter for mCherry was employed. To detect the emission for CFP and YFP, an emission filter cube with a 475/28 nm filter for CFP, a 495 nm long-pass dichroic mirror, and a 542/27 nm filter for YFP was used. Only the donor lifetime was measured for phasor FLIM-FRET either in the presence or absence of the FRET

acceptor. Optogenetic activation was performed with a supercontinuum laser using 445 nm or 488 nm excitation. Excitation occurred with a pixel dwell time of 0.1 ms and a duration of 30 frames, with each frame lasting ~7 s.

Confocal images of 256 x 256 pixel frame were obtained under each experimental condition, with a 100 μm motorized variable pinhole and a pixel dwell time of 0.1-0.4 ms. Acquired pixels were examined using the phasor plot. The VistaVision software (ISS, Inc., Champaign, IL) was used for image processing, display, and acquisition and allows for the specification of parameters such as pixel dwell time, image size, and resolution. The fitting algorithm and multi-phasor analysis were used for FLIM analysis. A median/gaussian smoothing filter and intensity-threshold filter were applied to enhance the display and analysis of membrane-localized lifetime species. Phasor FLIM can differentiate between signals originating from the background outside of the membrane and those within the membrane. The VistaVision software was used for determination of phase delays (φ) and modulation ratios (m) of the fluorescence signal in response to an oscillatory stimulus with a frequency of ω. Sine and cosine Fourier transforms of the phase histogram were performed, with consideration for the instrument response function (IRF) calibrated with Atto 425 (lifetime: 3.6 ns) and rhodamine 110 (lifetime: 4 ns) measured in solution, for 445 nm and 488 nm excitations, respectively.

The FRET trajectory function in the VistaVision software allowed for analysis of FLIM-FRET measurements (37). Three parameters were adjusted to ensure accurate results and optimize the fitting trajectory through both the unquenched donor and donor species affected by FRET. These parameters include the background contribution in the donor sample, unquenched donor contribution in the FRET sample, and the background contribution in the FRET sample. Background levels for both the donor sample and FRET sample were typically under 4%, which corresponds with the very low emission intensity observed in untransfected cells.

Animals and Dorsal Root Ganglion (DRG) Neuron Preparation

All procedures involving animals were approved by the Institutional Animal Care and Use Committee (IACUC) of Saint Louis University and adhered to the National Institutes of Health guidelines. Adult pathogen-free Sprague-Dawley rats (females, ~100 g; males, ~250 g; Envigo, Placentia, CA) were housed under a 12-hour light/dark cycle (lights on at 06:00 AM) in a temperature-controlled room (23 ± 3°C) with ad libitum access to food and water. All behavioral experiments were conducted by investigators blinded to treatment conditions.

Primary DRG neurons were isolated from naïve adult female rats (100 g), or adult male rats (250 g) subjected to nerve injury. Animals were deeply anesthetized, and the dorsal skin and underlying musculature were carefully dissected to expose the vertebral column. Dorsal root ganglia (DRGs) were isolated by removing the vertebral bone overlying the spinal cord, followed by excision and trimming of the DRG roots. Isolated DRGs were enzymatically digested in 3 mL of sterile, bicarbonate-free, serum-free DMEM (Catalog# 11965, Thermo Fisher Scientific, Waltham, MA) containing 3.125 mg/mL neutral protease (Catalog# LS02104, Worthington Biochemical Corp., Lakewood, NJ) and 5 mg/mL collagenase Type I (Catalog# LS004194, Worthington). Tissue digestion was carried out at 37°C for 45 minutes with gentle agitation. Following digestion, cells were centrifuged and resuspended in DRG culture medium consisting of DMEM supplemented with 10% fetal bovine serum, 30 ng/mL nerve growth factor, and 1% penicillin/streptomycin. Cells (~1.5×10^6) were plated onto 12-mm coverslips pre-coated with poly-D-lysine and laminin and maintained at 37°C in a humidified incubator with 5% CO_2 until experimentation.

Spared Nerve Injury (SNI) Surgery and Behavioral Testing

Rats were anesthetized using 5% isoflurane for induction and maintained at 2.5% during surgery. Animals were placed on a heating pad to maintain core body temperature, and areflexia was confirmed prior to incision. The surgical site on the right hindlimb was cleaned with chlorhexidine (applied twice), and a 2–3 cm incision was made along the lateral thigh. The biceps femoris muscle was bluntly retracted to expose the sciatic nerve and its three terminal branches. The common peroneal and tibial nerves were tightly ligated using 4–0 silk sutures and transected, while the sural nerve was left intact. The muscle was closed with 5–0 absorbable suture, and the skin was closed with surgical clips. Topical antibiotic ointment was applied, and animals were allowed to recover for 10 days before behavioral assessments.

Von Frey mechanical sensitivity testing was used to assess tactile allodynia. Testing was conducted in a blinded manner in a quiet, temperature-controlled room. Rats were acclimated to the testing environment in individual Plexiglas chambers placed on a wire mesh platform. Calibrated von Frey filaments were applied to the lateral plantar surface of the hindpaw, and the 50% paw withdrawal threshold was determined using the up-down method.

Patch-Clamp Electrophysiology

Electrophysiological recordings were performed in whole-cell configuration using an EPC10 amplifier and PATCHMASTER software (HEKA Elektronik), with data acquired at a sampling rate of 5 kHz. Recording pipettes were pulled from borosilicate glass capillaries using a P1000 puller (Sutter Instruments, Novato, CA) and had a resistance of 2.5-4 MΩ when filled. Precise positioning of pipettes was achieved using a Sutter MP-225A motorized micromanipulator. All recordings were conducted at ambient room temperature.

To record HCN channel currents in dorsal root ganglion (DRG) neurons, the internal pipette solution contained (in mM): 10 NaCl, 137 KCl, 4 Mg-ATP, 10 HEPES, and 1 EGTA, pH adjusted to 7.3 with KOH. The inclusion of 4 mM Mg-ATP was sufficient to preserve intracellular phosphoinositide levels, particularly $PI(4,5)P_2$, throughout the duration of recordings (52, 53). The extracellular solution consisted of (in mM): 154 NaCl, 5.6 KCl, 1 $MgCl_2$, 1 $CaCl_2$, 8 HEPES, and 10 D-glucose, titrated to pH 7.4 with NaOH. Series resistance was routinely maintained below 10 MΩ and compensated by 40%–70%. For the action potential measurements, whole-cell current clamp mode of PATCHMASTER was used instead of the voltage-clamp configuration for HCN current measurements. Spontaneous firing was measured with 0 pA current injection.

HCN current activation properties were assessed by measuring tail currents at −60 mV, following a series of test voltages from −40 mV to −140 mV in 10 mV increments. Leak-subtracted tail currents were normalized to the maximal amplitude and plotted to generate conductance-voltage (G–V) relationships. These data were fitted with a Boltzmann function: $G/G_{max} = 1/(1 + \exp[(V - V_{1/2})/V_S])$, where V is the test potential, $V_{1/2}$ is the voltage at which half-maximal activation occurs, and V_S is the slope factor. The slope factor was defined as $V_S = RT/zeF$, where R is the gas constant, T is the absolute temperature (297 K), F is the Faraday constant, e is the elementary charge, and z is the effective gating charge.

Statistics and Reproducibility

The data parameters were presented as the mean ± s.e.m. of n independent cells. Statistical significance was determined using the two-sided student's t test for comparison of two groups, or a one-way ANOVA test followed by a Tukey's post hoc test for comparison of more than two groups, denoted as $^*p < 0.05$ and $^{**}p < 0.01$ respectively.

ACKNOWLEDGEMENTS

We thank Donald W. Hilgemann (University of Texas Southwestern Medical Center) for advice and Erin N. Lessie for technical support. This research is supported by National Institute of General Medical Sciences R35GM154778 grant (to G.D.), R56HL169176 (to G.D.) and by the Doisy Fund (to G.D. and L.J.H.) of the Edward A. Doisy Department of Biochemistry and Molecular Biology at Saint Louis University School of Medicine. The Moutal lab is supported by startup funds from the Department of Pharmacology and Physiology, Saint Louis University, Institute for Drug & Biotherapeutic Innovation seed grant, National Institute of Neurological Disorders and Stroke R01NS119263 grant. Cartoons in figures were created using BioRender.

AUTHOR CONTRIBUTIONS

All Dai lab members contributed to the experimental design, data acquisition, and analysis. A.M. and N.L.A.D. supervised and performed the DRG neuron preparation and rat studies. G.D. wrote the manuscript.

COMPETING INTERESTS

The authors declare no competing interests.

REFERENCES

1. E. Sezgin, I. Levental, S. Mayor, C. Eggeling, The mystery of membrane organization: composition, regulation and roles of lipid rafts. *Nat Rev Mol Cell Biol* **18**, 361-374 (2017).
2. I. Levental, E. Lyman, Regulation of membrane protein structure and function by their lipid nano-environment. *Nat Rev Mol Cell Biol* **24**, 107-122 (2023).
3. F. Schmid, Physical mechanisms of micro- and nanodomain formation in multicomponent lipid membranes. *Biochim Biophys Acta Biomembr* **1859**, 509-528 (2017).
4. D. Lingwood, K. Simons, Lipid Rafts as a Membrane-Organizing Principle. *Science* **327**, 46-50 (2010).
5. S. L. Veatch, S. L. Keller, Organization in lipid membranes containing cholesterol. *Phys Rev Lett* **89**, 268101 (2002).
6. C. E. Cornell, A. Mileant, N. Thakkar, K. K. Lee, S. L. Keller, Direct imaging of liquid domains in membranes by cryo-electron tomography. *Proc Natl Acad Sci U S A* **117**, 19713-19719 (2020).
7. L. J. Handlin *et al.*, Membrane lipid nanodomains modulate HCN pacemaker channels in nociceptor DRG neurons. *Nat Commun* **15**, 9898 (2024).
8. C. Eggeling *et al.*, Direct observation of the nanoscale dynamics of membrane lipids in a living cell. *Nature* **457**, 1159-1162 (2009).
9. R. Ehehalt, P. Keller, C. Haass, C. Thiele, K. Simons, Amyloidogenic processing of the Alzheimer beta-amyloid precursor protein depends on lipid rafts. *J Cell Biol* **160**, 113-123 (2003).
10. R. J. Andrew *et al.*, Lack of BACE1 S-palmitoylation reduces amyloid burden and mitigates memory deficits in transgenic mouse models of Alzheimer's disease. *Proc Natl Acad Sci U S A* **114**, E9665-E9674 (2017).
11. G. Dai, Neuronal KCNQ2/3 channels are recruited to lipid raft microdomains by palmitoylation of BACE1. *J Gen Physiol* **154** (2022).
12. K. Fecchi *et al.*, Coronavirus Interplay With Lipid Rafts and Autophagy Unveils Promising Therapeutic Targets. *Front Microbiol* **11**, 1821 (2020).
13. D. Sviridov, Y. I. Miller, R. A. Ballout, A. T. Remaley, M. Bukrinsky, Targeting Lipid Rafts-A Potential Therapy for COVID-19. *Front Immunol* **11**, 574508 (2020).
14. P. Varshney, V. Yadav, N. Saini, Lipid rafts in immune signalling: current progress and future perspective. *Immunology* **149**, 13-24 (2016).
15. J. M. Navia-Pelaez *et al.*, AIBP regulates TRPV1 activation in chemotherapy-induced peripheral neuropathy by controlling lipid raft dynamics and proximity to TLR4 in dorsal root ganglion neurons. *Pain* **164**, e274-e285 (2023).
16. K. Wennerberg, K. L. Rossman, C. J. Der, The Ras superfamily at a glance. *J. Cell Sci.* **118**, 843-846 (2005).
17. A. Schaefer, N. R. Reinhard, P. L. Hordijk, Toward understanding RhoGTPase specificity: structure, function and local activation. *Small GTPases* **5**, 6 (2014).
18. X. Ma, Y. Zhao, Y. Daaka, Z. Nie, Acute activation of beta2-adrenergic receptor regulates focal adhesions through betaArrestin2- and p115RhoGEF protein-mediated activation of RhoA. *J Biol Chem* **287**, 18925-18936 (2012).
19. P. W. Oakes *et al.*, Optogenetic control of RhoA reveals zyxin-mediated elasticity of stress fibres. *Nat Commun* **8**, 15817 (2017).
20. A. J. Ridley, Rho family proteins: coordinating cell responses. *Trends Cell Biol* **11**, 471-477 (2001).
21. R. Eckenstaler, M. Hauke, R. A. Benndorf, A current overview of RhoA, RhoB, and RhoC functions in vascular biology and pathology. *Biochem Pharmacol* **206**, 115321 (2022).
22. C. Cheng *et al.*, Activated RhoA and peripheral axon regeneration. *Exp Neurol* **212**, 358-369 (2008).

23. K. Temporin *et al.*, IL-1β promotes neurite outgrowth by deactivating RhoA via p38 MAPK pathway. *Biochem Biophys Res Commun* **365**, 375-380 (2008).
24. M. Lehmann *et al.*, Inactivation of Rho signaling pathway promotes CNS axon regeneration. *J Neurosci* **19**, 7537-7547 (1999).
25. H. Neumann *et al.*, Tumor necrosis factor inhibits neurite outgrowth and branching of hippocampal neurons by a rho-dependent mechanism. *J Neurosci* **22**, 854-862 (2002).
26. J. Hu, M. E. Selzer, RhoA as a target to promote neuronal survival and axon regeneration. *Neural Regen Res* **12**, 525-528 (2017).
27. S. Quarta *et al.*, Sphingosine-1-Phosphate and the S1P(3) Receptor Initiate Neuronal Retraction via RhoA/ROCK Associated with CRMP2 Phosphorylation. *Front Mol Neurosci* **10**, 317 (2017).
28. D. W. Hilgemann *et al.*, Lipid signaling to membrane proteins: From second messengers to membrane domains and adapter-free endocytosis. *J Gen Physiol* **150**, 211-224 (2018).
29. V. Lariccia *et al.*, Massive calcium-activated endocytosis without involvement of classical endocytic proteins. *J Gen Physiol* **137**, 111-132 (2011).
30. D. W. Hilgemann, M. J. Lin, M. Fine, C. Deisl, On the existence of endocytosis driven by membrane phase separations. *Biochim Biophys Acta Biomembr* **1862**, 183007 (2020).
31. C. Deisl, O. W. Moe, D. W. Hilgemann, Constitutive Plasma Membrane Turnover in T-REx293 cells via Ordered Membrane Domain Endocytosis under Mitochondrial Control. *bioRxiv* 10.1101/2024.01.17.576124 (2024).
32. F. Laguia *et al.*, Massive endocytosis mechanisms are involved in uptake of HIV-1 particles by monocyte-derived dendritic cells. *Front Immunol* **15**, 1505840 (2024).
33. D. W. Hilgemann, M. Fine, Mechanistic analysis of massive endocytosis in relation to functionally defined surface membrane domains. *J Gen Physiol* **137**, 155-172 (2011).
34. T. Matsubara *et al.*, Heterogeneous Ganglioside-Enriched Nanoclusters with Different Densities in Membrane Rafts Detected by a Peptidyl Molecular Probe. *Langmuir* **37**, 646-654 (2021).
35. R. Sachl *et al.*, On multivalent receptor activity of GM1 in cholesterol containing membranes. *Biochim Biophys Acta* **1853**, 850-857 (2015).
36. F. Huang *et al.*, Multiple conformations of full-length p53 detected with single-molecule fluorescence resonance energy transfer. *Proc Natl Acad Sci U S A* **106**, 20758-20763 (2009).
37. M. A. Digman, V. R. Caiolfa, M. Zamai, E. Gratton, The phasor approach to fluorescence lifetime imaging analysis. *Biophys J* **94**, L14-16 (2008).
38. L. J. Handlin, G. Dai, Direct regulation of the voltage sensor of HCN channels by membrane lipid compartmentalization. *Nat Commun* **14**, 6595 (2023).
39. E. Hinde, M. A. Digman, K. M. Hahn, E. Gratton, Millisecond spatiotemporal dynamics of FRET biosensors by the pair correlation function and the phasor approach to FLIM. *Proc Natl Acad Sci U S A* **110**, 135-140 (2013).
40. L. Malacrida, S. Ranjit, D. M. Jameson, E. Gratton, The Phasor Plot: A Universal Circle to Advance Fluorescence Lifetime Analysis and Interpretation. *Annu Rev Biophys* **50**, 575-593 (2021).
41. S. Ranjit, L. Malacrida, D. M. Jameson, E. Gratton, Fit-free analysis of fluorescence lifetime imaging data using the phasor approach. *Nat Protoc* **13**, 1979-2004 (2018).
42. C. Wilde, H. Genth, K. Aktories, I. Just, Recognition of RhoA by Clostridium botulinum C3 exoenzyme. *J Biol Chem* **275**, 16478-16483 (2000).
43. I. Just *et al.*, Purification and characterization of an ADP-ribosyltransferase produced by Clostridium limosum. *J Biol Chem* **267**, 10274-10280 (1992).
44. G. Flatau *et al.*, Toxin-induced activation of the G protein p21 Rho by deamidation of glutamine. *Nature* **387**, 729-733 (1997).
45. G. Schmidt *et al.*, Gln 63 of Rho is deamidated by Escherichia coli cytotoxic necrotizing factor-1. *Nature* **387**, 725-729 (1997).
46. T. Schmidt *et al.*, ProteomicsDB. *Nucleic Acids Res* **46**, D1271-D1281 (2018).

47. J. Myeong, C. G. Park, B. C. Suh, B. Hille, Compartmentalization of phosphatidylinositol 4,5-bisphosphate metabolism into plasma membrane liquid-ordered/raft domains. *Proc Natl Acad Sci U S A* **118** (2021).
48. G. R. Chichili, W. Rodgers, Clustering of membrane raft proteins by the actin cytoskeleton. *J Biol Chem* **282**, 36682-36691 (2007).
49. G. Guntas *et al.*, Engineering an improved light-induced dimer (iLID) for controlling the localization and activity of signaling proteins. *Proc Natl Acad Sci U S A* **112**, 112-117 (2015).
50. H. Inaba, Q. Miao, T. Nakata, Optogenetic control of small GTPases reveals RhoA mediates intracellular calcium signaling. *J Biol Chem* **296**, 100290 (2021).
51. P. R. O'Neill *et al.*, Membrane Flow Drives an Adhesion-Independent Amoeboid Cell Migration Mode. *Dev Cell* **46**, 9-22 e24 (2018).
52. E. K. Mahlandt *et al.*, Opto-RhoGEFs, an optimized optogenetic toolbox to reversibly control Rho GTPase activity on a global to subcellular scale, enabling precise control over vascular endothelial barrier strength. *Elife* **12** (2023).
53. E. Wagner, M. Glotzer, Local RhoA activation induces cytokinetic furrows independent of spindle position and cell cycle stage. *J Cell Biol* **213**, 641-649 (2016).
54. L. Benedetti *et al.*, Light-activated protein interaction with high spatial subcellular confinement. *Proc Natl Acad Sci U S A* **115**, E2238-E2245 (2018).
55. P. R. O'Neill, V. Kalyanaraman, N. Gautam, Subcellular optogenetic activation of Cdc42 controls local and distal signaling to drive immune cell migration. *Mol Biol Cell* **27**, 1442-1450 (2016).
56. R. Kristelly, G. Gao, J. J. Tesmer, Structural determinants of RhoA binding and nucleotide exchange in leukemia-associated Rho guanine-nucleotide exchange factor. *J Biol Chem* **279**, 47352-47362 (2004).
57. J. N. Iuliano *et al.*, Unraveling the Mechanism of a LOV Domain Optogenetic Sensor: A Glutamine Lever Induces Unfolding of the Jalpha Helix. *ACS Chem Biol* **15**, 2752-2765 (2020).
58. M. Jaiswal, R. Dvorsky, M. R. Ahmadian, Deciphering the molecular and functional basis of Dbl family proteins: a novel systematic approach toward classification of selective activation of the Rho family proteins. *J Biol Chem* **288**, 4486-4500 (2013).
59. I. Decosterd, C. J. Woolf, Spared nerve injury: an animal model of persistent peripheral neuropathic pain. *Pain* **87**, 149-158 (2000).
60. R. B. Robinson, S. A. Siegelbaum, Hyperpolarization-activated cation currents: from molecules to physiological function. *Annu Rev Physiol* **65**, 453-480 (2003).
61. H. Raghu *et al.*, Localization of uPAR and MMP-9 in lipid rafts is critical for migration, invasion and angiogenesis in human breast cancer cells. *BMC Cancer* **10**, 647 (2010).
62. J. B. Larsen *et al.*, Membrane curvature enables N-Ras lipid anchor sorting to liquid-ordered membrane phases. *Nat Chem Biol* **11**, 192-194 (2015).
63. F. J. Rios *et al.*, Uptake of oxLDL and IL-10 production by macrophages requires PAFR and CD36 recruitment into the same lipid rafts. *PLoS One* **8**, e76893 (2013).
64. L. Stirling, M. R. Williams, A. D. Morielli, Dual roles for RHOA/RHO-kinase in the regulated trafficking of a voltage-sensitive potassium channel. *Mol Biol Cell* **20**, 2991-3002 (2009).
65. O. Pochynyuk, A. Staruschenko, V. Bugaj, L. Lagrange, J. D. Stockand, Quantifying RhoA facilitated trafficking of the epithelial Na+ channel toward the plasma membrane with total internal reflection fluorescence-fluorescence recovery after photobleaching. *J Biol Chem* **282**, 14576-14585 (2007).
66. M. Rousset *et al.*, Regulation of neuronal high-voltage activated Ca_V2 Ca^{2+} channels by the small GTPase RhoA. *Neuropharmacology* **97**, 201-209 (2015).
67. D. Mehta *et al.*, RhoA interaction with inositol 1,4,5-trisphosphate receptor and transient receptor potential channel-1 regulates Ca^{2+} entry. Role in signaling increased endothelial permeability. *J Biol Chem* **278**, 33492-33500 (2003).
68. J. W. Hao *et al.*, CD36 facilitates fatty acid uptake by dynamic palmitoylation-regulated endocytosis. *Nat Commun* **11**, 4765 (2020).

69. D. W. Hilgemann, M. Fine, M. E. Linder, B. C. Jennings, M. J. Lin, Massive endocytosis triggered by surface membrane palmitoylation under mitochondrial control in BHK fibroblasts. *Elife* **2**, e01293 (2013).
70. M. Simunovic, G. A. Voth, Membrane tension controls the assembly of curvature-generating proteins. *Nat Commun* **6**, 7219 (2015).
71. A. Diz-Munoz, D. A. Fletcher, O. D. Weiner, Use the force: membrane tension as an organizer of cell shape and motility. *Trends Cell Biol* **23**, 47-53 (2013).
72. I. Levental, D. Lingwood, M. Grzybek, U. Coskun, K. Simons, Palmitoylation regulates raft affinity for the majority of integral raft proteins. *Proc Natl Acad Sci U S A* **107**, 22050-22054 (2010).
73. M. J. Lin *et al.*, Massive palmitoylation-dependent endocytosis during reoxygenation of anoxic cardiac muscle. *Elife* **2**, e01295 (2013).
74. O. Rocks *et al.*, An acylation cycle regulates localization and activity of palmitoylated Ras isoforms. *Science* **307**, 1746-1752 (2005).
75. I. Navarro-Lerida *et al.*, A palmitoylation switch mechanism regulates Rac1 function and membrane organization. *EMBO J* **31**, 534-551 (2012).
76. Y. Fukata, T. Murakami, N. Yokoi, M. Fukata, Local Palmitoylation Cycles and Specialized Membrane Domain Organization. *Curr Top Membr* **77**, 97-141 (2016).
77. G. Dai, H. Yu, M. Kruse, A. Traynor-Kaplan, B. Hille, Osmoregulatory inositol transporter SMIT1 modulates electrical activity by adjusting PI(4,5)P_2 levels. *Proc Natl Acad Sci U S A* **113**, E3290-3299 (2016).
78. R. A. Colyer, C. Lee, E. Gratton, A novel fluorescence lifetime imaging system that optimizes photon efficiency. *Microsc Res Tech* **71**, 201-213 (2008).